Surface Discretisation Effects on 3D Printed Surface Appearance

Alina Pranovich[1], Sasan Gooran[1], Jeppe Revall Frisvad[2], and Daniel Nyström[1]

[1] Linköping University, Norrköping, Sweden
alina.pranovich@liu.se, sasan.gooran@liu.se, daniel.nystrom@liu.se
[2] Technical University of Denmark, Kongens Lyngby, Denmark
jerf@dtu.dk

Abstract. The spatial resolution of 3D printing is finite. The necessary discretisation of an object before printing produces a step-like surface structure that influences the appearance of the printed objects. To study the effect of this discretisation on specular reflections, we print surfaces at various oblique angles. This enables us to observe the step-like structure and its influence on reflected light. Based on the step-like surface structure, we develop a reflectance model describing the redistribution of the light scattered by the surface, and we study dispersion effects due to the wavelength dependency of the refractive index of the material. We include preliminary verification by comparing model predictions to photographs for different angles of observation.

Keywords: BRDF · 3D printing · gloss · material appearance.

1 Introduction

The appearance of objects with known optical properties can be modelled with different rendering techniques [2]. An aspect of particular interest is color appearance assessment under a certain illumination [10,15]. While one might expect manufactured surfaces to be perfectly smooth, each manufacturing process imprints its characteristics on the object including mechanical properties [9] and appearance [2]. An important part of object appearance is gloss (reflection highlights) [5]. Highlights are directly affected by the surface structure as it changes the magnitude and directions of specular light reflections. Even with the same raw material, the surface can be perceived as having slightly different colour caused by different manufacturing technology and surface finishing. One example is objects produced by 3D printing [12].

In 3D printing, the surface requires discretisation. For example, in Fused Deposition Modelling 3D printing (FDM), the object is created by applying melted material in a layer-by-layer flow. Any oblique surface to be printed will

be affected by this slicing. As a result, any oblique surface will be approximated by a staircase-like shape. In this paper, we investigate plane surfaces of FDM-printed wedges and the effect of the surface discretisation on the appearance for different wedge angles. For this, we consider wedges as schematically shown in Fig. 1, a–c). We limit our study to surface reflection only. Once the scattering of light by the surface has been modelled, it can be combined with subsurface scattering using volumetric light transport simulation [6,7].

Reflectance models for ridges such as the symmetric V-groove cavity [17] have been studied for a long time. Most models however study the bidirectional reflectance distribution function (BRDF) resulting from a statistical distribution of microfacet normals [14], where the microfacets form V-grooves. Multiple reflections were recently included in this type of model [16], also for nonsymmetric V-grooves [8], but our interest is reflectance from a periodic ridged surface rather than a distribution of microfacets. The symmetric V-groove model was recently investigated for a periodic ridged surface [13]. Our staircase-like ridges are, however, both nonsymmetric and periodic. In other related work, a BRDF was developed for ridged surfaces like ours [11]. There, the authors focused on single scattering and incorporated statistical distribution of surface normals together with the ridges to model surface imperfection. We include retroreflection due to two scattering events, and we parameterise our model in a different way to make the model suitable for the staircase structures observed in 3D printing. A model for retrieval of a shading normal following the step-like structure of 3D printed objects has also been suggested [3]. This model, however, was intended for close-up rendering of the layers rather than calculation of a BRDF.

2 Method

Angular redistribution of incident light after single or multiple reflections can be quantitatively estimated with geometrical ray optics, together with the Fresnel equations [1]. The range of validity of this approach is determined by two main assumptions. First, the structures must be substantially larger than the wavelength (considering visible light, 380-780 nm) to prevent visible interference effects. Hence, at least a few micrometers. Second, the size of individual surface elements shall not substantially exceed the resolution of the human eye, which, for example, at a viewing distance of 50 cm is on the order of 150 µm.

For the wedges described above, together with a given printing resolution, the unit cell considered for calculation is defined as illustrated in Fig. 1, e). A unit cell is chosen as a concave right-angled structure with two slopes defined by the vertical printing resolution. The length of one side corresponds to the printing layer thickness l_1 (vertical printing resolution). The second side l_2 is given by l_1 and the wedge angle β_2. The side corresponding to the layer thickness l_1 forms the angle $\beta_1 = 90° - \beta_2$ with the wedged plane (Fig. 1, a,e). We thus have

$$l_2 = \frac{l_1 \sin \beta_1}{\sin \beta_2} = l_1 \cot \beta_2 \,. \tag{1}$$

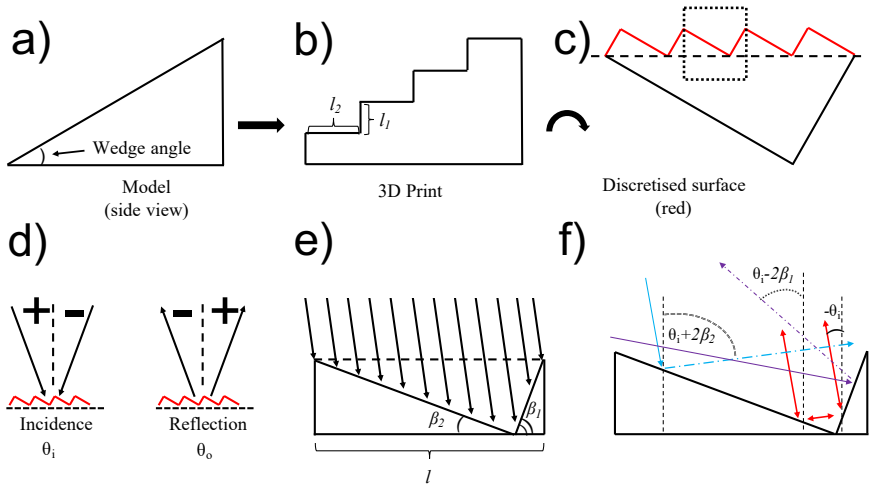

Fig. 1. a): Side view of a 3D model of a wedge with defined wedge angle. b): Side view of resulting printed wedges with discretised surface, l_1 is the layer thickness in the z direction, l_2 is a step length in the y direction. c): Examined discretised surface. The unit cell chosen for calculation is highlighted with a dashed square. d): Sign conventions for the angles of incidence and observation with respect to the surface normal. e): The surface unit cell considered in calculations is illuminated by rays hitting the section of length l between the tips of the slopes. f): Exemplary ray reflection scenarios. Each case of double reflection is a retroreflection due to the mutually perpendicular slopes.

It is sufficient to consider a one-dimensional unit cell as the surface is constant in the perpendicular lateral direction. The relation of the angle of incidence θ_i and the angle of observation θ_o to 3D direction vectors describing the light-view configuration and the surface geometry is covered by Luongo et al. [11].

Incident illumination is defined through a number of rays hitting the section of the length $l = \sqrt{l_1^2 + l_2^2}$ between the tips of the slopes. By assuming that illumination consists of a number of rays homogeneously distributed with a certain density in the plane defined by the unit cell, we can express radiance of incident light through the projection of any segment within the unit cell onto the rayfront. The radiance illuminating each slope is then expressed through their projections:

$$r_1 = l_1 \max\{\sin(\beta_2 + \theta_i), 0\} + l_2 \min\{\cos(\beta_2 + \theta_i), 0\} \tag{2}$$

$$r_2 = l_2 \max\{\cos(\beta_2 + \theta_i), 0\} + l_1 \min\{\sin(\beta_2 + \theta_i), 0\}\,. \tag{3}$$

The max and min functions help us to avoid listing three different cases. When $-\beta_2 \leq \theta_i \leq \beta_1$, the first terms in the two expressions are nonzero, while the second terms are zero. On the other hand, when $\theta_i < -\beta_2$, we have $r_1 = 0$ and both terms active for r_2. The opposite is the case for $\theta_i > \beta_1$. We also recall Lambert's cosine law: the more grazing the angle of incidence, the smaller the

density of incident rays. The irradiance is thus proportional to the cosine of the angle of incidence, but this term is not part of the BRDF.

Light can leave the surface after being reflected once by any of the slopes or after a double reflection. Due to the mutually perpendicular slopes, each case where double reflection occurs is a retroreflection, with the scattered light direction coinciding with the direction of incidence (independently of the wedge angle). By letting our model account for this retroreflection, masking effects do not need to be considered explicitly, but are intrinsically accounted for. One angle of incidence θ_i can be associated with several scattering angles. Depending on the position of an incident ray along the slopes, light can be reflected with scattering angle θ_o:

$$\text{from left slope} : \theta_o = \theta_i + 2\beta_2 \tag{4}$$

$$\text{from right slope} : \theta_o = \theta_i - 2\beta_1 \tag{5}$$

$$\text{retroreflection} : \quad \theta_o = -\theta_i \,. \tag{6}$$

The convention regarding the sign of θ_i and θ_o still follows Fig. 1, d). For a given angle of incidence, we calculate the proportion of the rays being reflected once or twice. Those proportions are expressed through the projections of the corresponding sections onto the rayfront. We can use θ_o from Eqs. (4–5) to get the direction of the incident light after the first reflection. Retroreflection occurs for the part of the first reflection being incident on the other slope. Insertion of the new directions in Eqs. (2-3) then provides the desired projections. For $-\beta_2 < \theta_i \leq \beta_1 - \beta_2$, all rays hitting the right slope will be retroreflected. The rays hitting the left slope will be partially directly reflected and partially retroreflected. The direction of the light after reflection in the left slope is $180° - \theta_i - 2\beta_2$. Inserting this direction of incidence in Eq. (2), we get the projection of the part of the left slope from which retroreflection occurs:

$$r_{21} = l_1 \sin(\beta_2 + \theta_i) \,. \tag{7}$$

Similar considerations apply for $\beta_1 - \beta_2 < \theta_i < \beta_1$. Here, all rays hitting the left slope will be retroreflected. The part of the rays falling on the right slope and being retroreflected is given by

$$r_{12} = l_2 \cos(\beta_2 + \theta_i) \,. \tag{8}$$

For angles of incidence satisfying $\theta_i > \beta_1$ or $\theta_i < -\beta_2$, only direct reflection occurs, which we calculate using Eqs. (2–3). The proportion of scattered light in each direction can have a value between 0 and $l \cos\theta_i$. We thus represent the proportions as reflectance ratios through division by $l \cos\theta_i$.

In addition to geometric considerations, the material refractive index influences the reflections of the individual slope surfaces. We calculate bidirectional reflectances using the Fresnel equations with tabulated wavelength-dependent refractive indices for the 3D printing materials obtained from spectroscopic ellipsometry. P- and S-polarised light is considered separately. For our final results, we use unpolarised light incident in the plane depicted in Fig. 1. The reflectance

is then half of each type of polarisation (also in the case of retroreflection as the plane of incidence is the same for both reflections). The amount of light entering the material is given by one minus the Fresnel reflectance. This refracted light can be used with a model for volumetric light transport [6,7] or subsurface scattering [4] to compute the full appearance of the wedge beyond predictions by our model. In this paper, we focus on the surface reflectance, which in terms of appearance attributes can be interpreted as gloss and colour of gloss. In order to model surface appearance under a certain viewing angle, light from all angles of incidence reflected into the desired viewing direction is integrated.

3 Results and Discussion

The described approach was used to predict reflectance properties of wedges printed with a fused deposition modelling (FDM) printer. Black polylactide (PLA) filament was used. Slope angles of the wedges were set to the values 10°, 20°, 30°, 40°, 45°, and 60°. Examples of printed wedges with 10° and 45° (side view) are shown in Fig. 2. The footprint of each slope was $2 \times 2\,\mathrm{cm}^2$. The num-

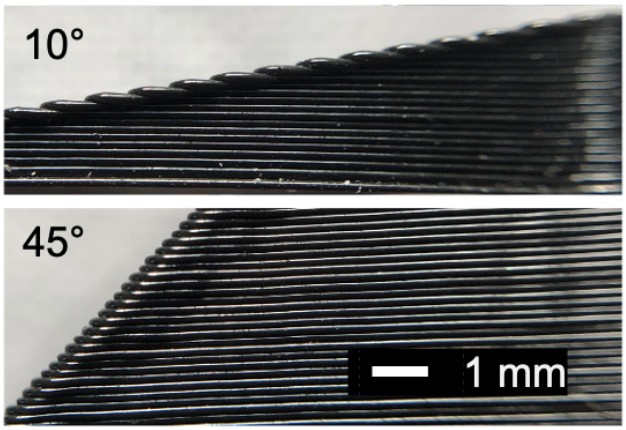

Fig. 2. Side view of printed wedges with 10° (top) and 45° (bottom) wedge angle.

bers of layers needed for each print were obtained after slicing the models with defined layer thickness (resolution in z direction). Larger slope angles resulted in a larger number of layers needed. Thus the step in y direction was smaller for the higher slope angles. Table 1 summarises used and calculated parameters.

We computed the reflectance by combining the pure geometrical effect with the Fresnel angular reflectance for each angle of incidence and reflection. Results at 550 nm are shown in Fig. 3. For the refractive index, a representative value of $n = 1.46$ for PLA has been chosen. The wavelength-dependent values of the

Table 1. 3D printing parameters. The layer thickness (z-step) was 150 µm.

wedge angle, °	10	20	30	40	45	60
number of layers	22	47	75	109	130	225
y-step, µm	909	426	267	183	154	89

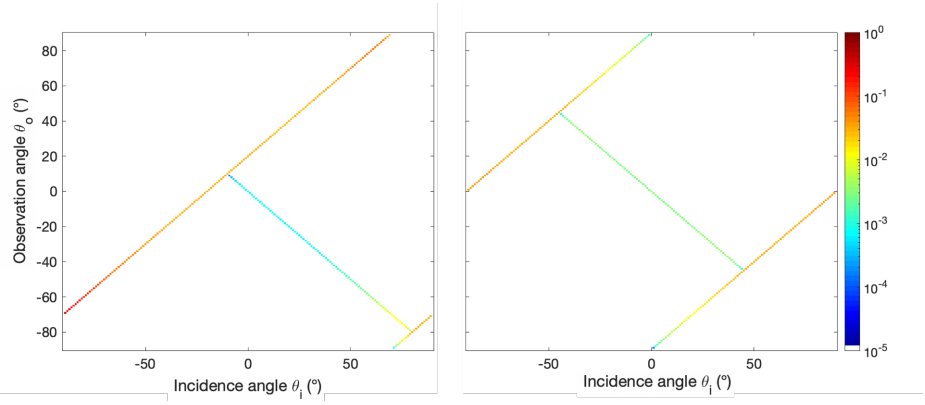

Fig. 3. Bidirectional reflectance (BRDF values) of wedges with wedge angles 10° (left) and 45° (right) for unpolarised incident light, calculated for 550 nm.

refractive index were obtained by spectroscopic ellipsometry and are shown in Fig. 4. As the reflectance values have been calculated for a one-dimensional surface cross-section, i.e. one plane of incidence and reflection, they represent an in-plane BRDF of the printed surface.

Characteristic patterns can be observed in the diagrams: The straight line $\theta_o = -\theta_i$ corresponds to retroreflection. The other two lines represent direct reflections from the two slopes, l_1 and l_2. Retroreflection is weaker because it involves two reflections. Retroreflection is not possible for $\theta_i < -\beta_2$ or $\theta_i > \beta_1$. The top-left line represents direct reflection from the left slope and the bottom-right line corresponds to direct reflection from the right slope. The intensity of the direct reflectances becomes weaker when also retroreflection is possible. Otherwise, the radiance distribution along the lines is a result of both the Fresnel reflectances and the geometrically determined proportions.

Considering light incident from all directions (diffuse lighting), the reflected contributions towards a given viewing angle can be accumulated (by integrating over all angles of incidence). An example is shown in Fig. 5. Here, characteristic peaks for certain angles of observation of each wedge can be observed. The peaks correspond to the situation when the longer slope is being illuminated under shallow angles. For example, for a 10° wedge with $\beta_2 = 10°$, $\beta_1 = 80°$, this occurs when θ_i is close to $-90°$ and hence, θ_o approaches $-90° + 2\beta_2$ (here $-70°$). From Fresnel equations, larger angles of incidence (with respect to the slope's surface normal) lead to the higher reflectance values (for angles greater than Brewster's angle). However, there is no contribution if $\theta_i = \pm 90°$. This causes a minimum at

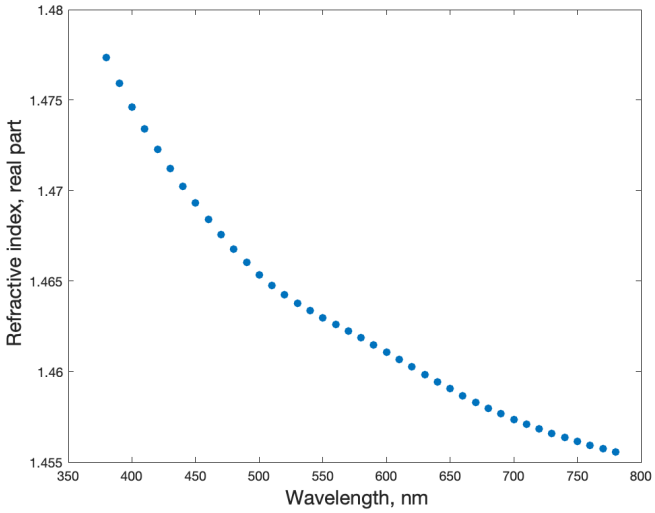

Fig. 4. Real part of the refractive index of PLA for wavelengths in the visible as obtained from spectroscopic ellipsometry measurements. Measured with a Dual-Rotating-Compensator ellipsometer RC2 by J.A. Woolam.

$\theta_o = -90° + 2\beta_2$. For wedge angles larger than 45° ($\beta_1 < 45°$), there is a strong contribution of light reflected at shallow angles directly off the right slope. This happens for θ_i approaching +90° and θ_o approaching $90° - 2\beta_1$. Comparing different wedge angles in Fig. 5, the longest printing step in y-direction was made in the case of the 10° wedge angle. Therefore the contribution to the peak value is the highest in this case, while the peak is least pronounced for 45°. Furthermore, as expected, the BRDF for the wedge angle 45° is symmetric with respect to $\theta_o = 0°$, as the unit cell is mirror symmetric. Similarly, the BRDFs of 30° and 60° wedges are mutually symmetric. For comparison, we calculated also the spectral reflectance for a plane surface which is shown in Fig. 5.

3.1 Spectral dependencies and appearance interpretation

In order to be able to interpret calculated light quantities as appearance attributes, the above described calculation has to be carried out for each wavelength of the visible spectrum (380 to 780 nm) separately because the refractive index is dispersive. Accumulated reflectance spectra for a given viewing direction were calculated after integrating over all incidence angles. An example of spectral reflectance for viewing angle 0° is shown in Fig. 6. Assuming a certain illuminant (e.g. D65), integrated reflected (scattered) radiance spectra towards a given angle of observation can be calculated and interpreted as surface contribution to the overall appearance. Interpretation of the colour under standard illuminants D65 and A is demonstrated in Fig. 7. The radiance changes with

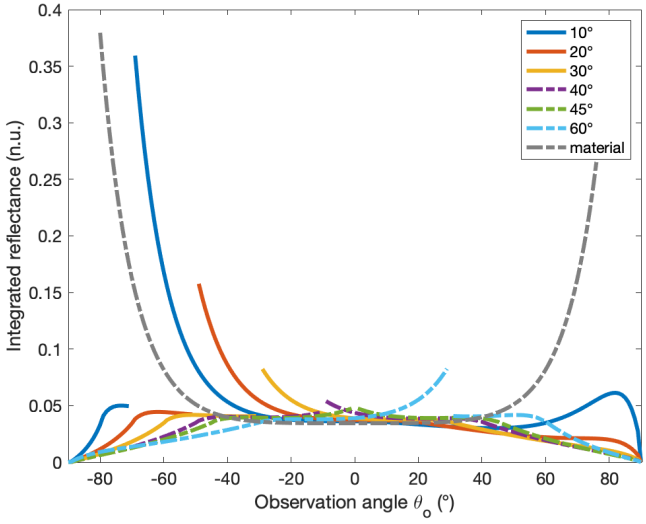

Fig. 5. Reflectance for different angles of observation. Calculated by integrating bidirectional reflectances (Fig. 3) over all angles of incidence $\theta_i \in [-90°, 90°]$ (no cosine weights). The legend displays the wedge angle. For comparison, we also show the values for direct specular reflectance of a perfectly planar surface (gray dash-dotted line called material in the legend). Data has been computed for 550 nm. The discontinuities occur when the incidence angle reaches $\pm 90°$.

varying viewing angle. Nevertheless, the redistributed specular reflections represent mostly a colour of the light source. As can be seen in Fig. 6, the reflectance is relatively uniform over the visible spectrum.

3.2 Including surface imperfections

Real surfaces contain rough details. In the case of the studied printed wedges, each individual slope surface is rough, also the edges of the layers are not perfectly sharp, but are to a certain degree round. Those two factors lead to statistically fluctuating angular deviation of scattered radiation, which introduces the diffusion and blurring of specular reflection. Additionally, the finite size of specimen and light source induce an angular spread. Furthermore, angular deviations can be observed for light that is incident from outside the plane of interest depicted in Fig. 1. All these factors can be represented through applying a convolution with Gaussian broadening to the computed BRDF. Fig. 8 shows the resulting scattered light angular distribution after applying convolution representing additional angular spread of reflection caused by surface roughness.

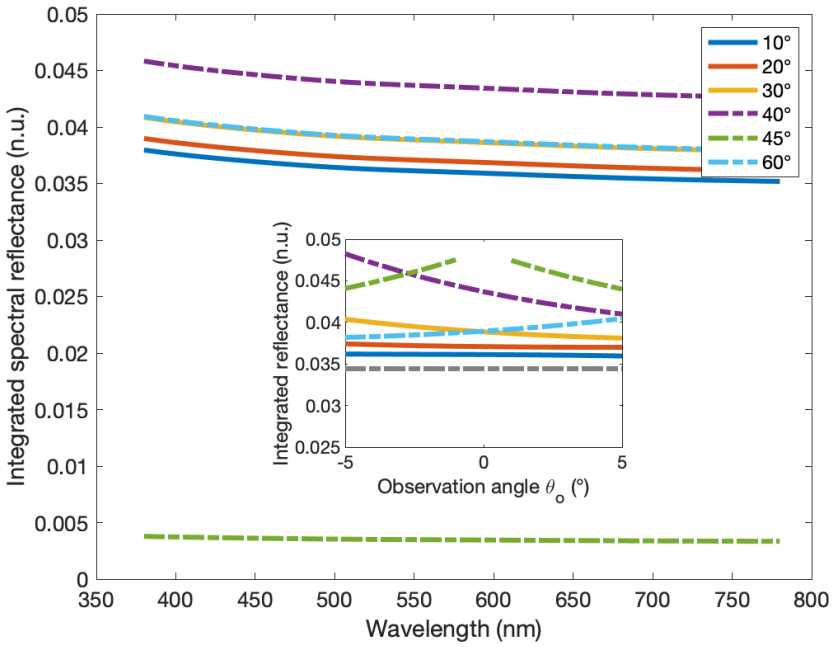

Fig. 6. Calculated reflectance spectra for 6 wedges (angles in the legend) using an "all-to-normal" configuration, where the bidirectional reflectance is integrated over all angles of incidence with a 0° angle of observation (along the normal direction). For comparison, the insert shows a close-up of Fig. 5 around $\theta_o = 0°$.

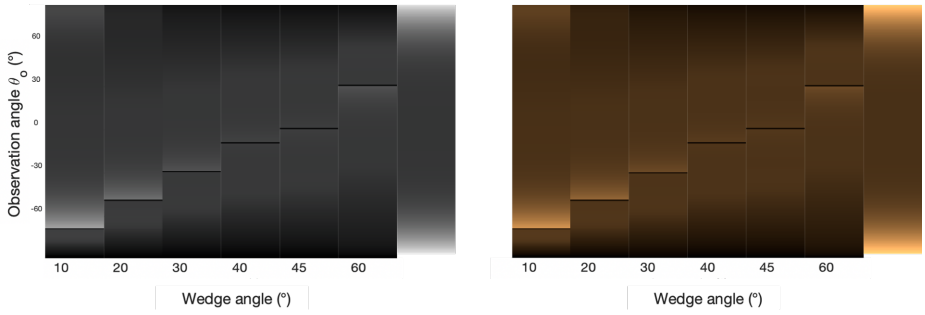

Fig. 7. Colour representation of integrated incidence light scattered towards different viewing angles. Example for the wedges with 10° to 60° angles and standard illuminants D65 (left) and A (right). For comparison, colour representation was also calculated for a plane surface (on the right side of each series). The figure demonstrates the pure colour effect from the surface, i.e. modified glossy reflections from the discretised surface.

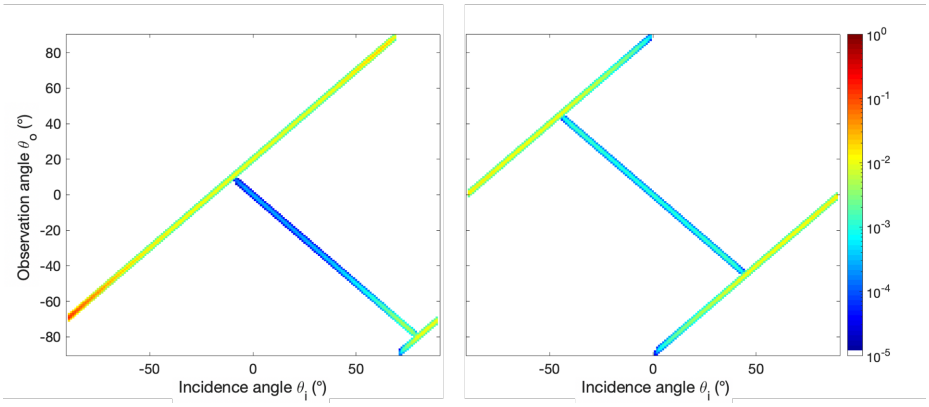

Fig. 8. BRDF values for wedges with 10° (left) and 45° (right) wedge angles printed with PLA after applying a convolution with Gaussian broadening (standard deviation of 5°). Calculated for 550 nm.

3.3 Comparison with photographic images

As a first attempt at verifying our approach, we compare the computed predictions to real visual impressions. For this purpose, a series of photographs was prepared. A small point-like LED light source was placed in 50 cm distance from the specimen. Photographs were taken at different angles at 90 cm distance with 135 mm objective and the following setting: ISO 100, exposure time 1 second and aperture 5.6. Figure 9 compares theoretical expectations with real appearance. The main quality that varies with changing viewing angle is the brightness which is casued by the redistribution of specular reflections. Despite of large scattering between the pictures, the general trend can be observed. Apparently, the real structures reveal large angular broadening. Remarkably, the 10° wedge has a generally darker appearance than the other ones. Also, the reflectances of 30° and 60° wedges differ from each other while the model predicts symmetric behaviour. The unit cells for both configurations have the same geometry, however the size of the unit cell decreases with the wedge angle. The unit cell of the 30° wedge is approximately 1.7 times bigger than that of the 60° one. As a conclusion, the absolute unit size plays a role in the appearance of the oblique 3D printed surfaces. A possible explanation is the impact of the real (rounded) edges of the printed layers (cf. Fig. 2). If the unit cell size approaches the curvature radius, those edges will dominate the scattering characteristics. Another consequence of large angular broadening for structures with smaller unit cells is the bright intensity scattered towards −80° for wedge angles around 40° as seen in the photographs. For example, for the 45° wedge, we would expect a direct reflection toward −90° which would not be observable. The brightness at −80° may result from the discussed angular broadening by imperfections like the round edges.

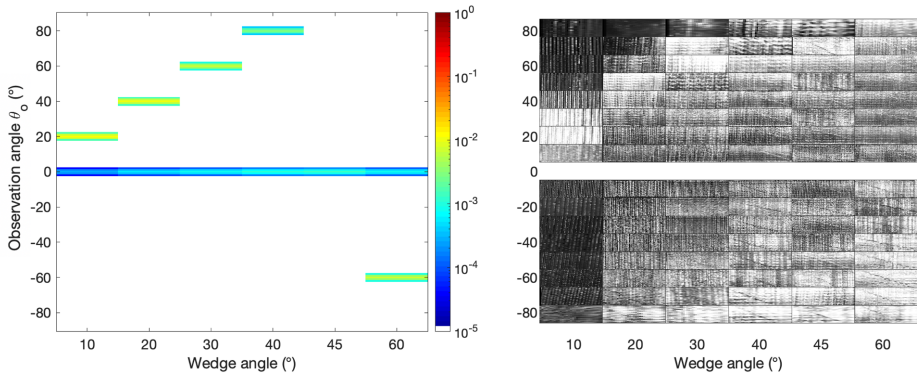

Fig. 9. Reflectance towards different angles with angle of incidence 0° for 6 different wedges. Left: computation similar to Fig. 8 after applying convolution with Gaussian distribution. Right: Gray-scaled photographs of the printed wedges taken at different angles. The higher reflectivity lines can be immediately recognized by increased brightness. Note that no pictures were taken for the 0° angle of observation.

4 Summary

In this work, the effects of oblique surfaces created with 3D printing on the object's appearance were studied. Due to the limited printing resolution, these surfaces are discretised according to the surface inclination. Using geometrical optics, shadowing effects and angular redistribution of specular reflections were modelled. Geometrical considerations were complemented by calculating wavelength dependent reflectance. The so calculated reflectances allowed us to predict the surface contribution to the object appearance, especially for highly absorbing materials. The approach was used to compute the colour tone of black material under a certain illuminant for different viewing angles. A series of wedges was 3D printed using FDM technique and black PLA filament. A comparison of model-predicted scattering with photographs taken at different viewing angles indicates reasonable correspondance in particular for those wedges with coarser discretisation. Such imperfections as rounded edges are not discribed by the model but have strong impact on surfaces with finer discretisation. For future work, we suggest a study of other aspects such as diffuse scattering by surface microfacets and subsurface scattering in a translucent print material.

Acknowledgment

Funded by the Horizon 2020 programme of the European Union. Grant # 814158.

References

1. Born, M., Wolf, E.: Principles of Optics: Electromagnetic Theory of Propagation, Interference and Diffraction of Light. Cambridge University Press, seventh (expanded) edn. (1999)
2. Dorsey, J., Rushmeier, H., Sillion, F.: Digital Modeling of Material Appearance. Elsevier (2010)
3. Eiriksson, E.R., Pedersen, D.B., Frisvad, J.R., Skovmand, L., Heun, V., Maes, P., Aanæs, H.: Augmented reality interfaces for additive manufacturing. In: Image Analysis (SCIA 2017). Lecture Notes in Computer Science, vol. 10269, pp. 515–525. Springer (2017)
4. Frisvad, J.R., Hachisuka, T., Kjeldsen, T.K.: Directional dipole model for subsurface scattering. ACM Transactions on Graphics **34**(1), 5:1–5:12 (November 2014)
5. Ged, G., Obein, G., Silvestri, Z., Le Rohellec, J., Viénot, F.: Recognizing real materials from their glossy appearance. Journal of Vision **10**(9), 18:1–18:17 (2010)
6. Hašan, M., Ramamoorthi, R.: Interactive albedo editing in path-traced volumetric materials. ACM Transactions on Graphics **32**(2), 11:1–11:11 (2013)
7. Křivánek, J., Georgiev, I., Hachisuka, T., Vévoda, P., Šik, M., Nowrouzezahrai, D., Jarosz, W.: Unifying points, beams, and paths in volumetric light transport simulation. ACM Transactions on Graphics **33**(4), 103:1–103:13 (2014)
8. Lee, J.H., Jarabo, A., Jeon, D.S., Gutierrez, D., Kim, M.H.: Practical multiple scattering for rough surfaces. ACM Transactions on Graphics **37**(6), 275:1–275:12 (2018)
9. Loflin, W.A., English, J.D., Borders, C., Harris, L.M., Moon, A., Holland, J.N., Kasper, F.K.: Effect of print layer height on the assessment of 3D-printed models. American Journal of Orthodontics and Dentofacial Orthopedics **156**(2), 283–289 (2019)
10. Luo, R.: Colour appearance assessment. Journal of the Society of Dyers and Colourists **112**(3), 72–74 (1996)
11. Luongo, A., Falster, V., Doest, M.B., Li, D., Regi, F., Zhang, Y., Tosello, G., Nielsen, J.B., Aanæs, H., Frisvad, J.R.: Modeling the anisotropic reflectance of a surface with microstructure engineered to obtain visible contrast after rotation. In: Proceedings of ICCVW 2017. pp. 159–165 (2017)
12. Luongo, A., Falster, V., Doest, M.B., Ribo, M.M., Eiriksson, E.R., Pedersen, D.B., Frisvad, J.R.: Microstructure control in 3D printing with digital light processing. Computer Graphics Forum **39**(1), 347–359 (February 2020)
13. Saint-Pierre, D., Chavel, P., Simonot, L., Hébert, M.: Angular reflectance model for ridged specular surfaces, with comprehensive calculation of inter-reflections and polarization. Journal of the Optical Society of America A **36**(11), C51–C61 (2019)
14. Torrance, K.E., Sparrow, E.M.: Theory for off-specular reflection from roughened surfaces. Journal of the Optical Society of America **57**(9), 1105–1114 (September 1967)
15. Xiao, B., Walter, B., Gkioulekas, I., Zickler, T., Adelson, E., Bala, K.: Looking against the light: How perception of translucency depends on lighting direction. Journal of Vision **14**(3), 17:1–17:22 (2014)
16. Xie, F., Hanrahan, P.: Multiple scattering from distributions of specular V-grooves. ACM Transactions on Graphics **37**(6), 276:1–276:14 (2018)
17. Zipin, R.B.: The apparent thermal radiation properties of an isothermal V-groove with specularly reflecting walls. Journal of Research of the National Bureau of Standards - C. Engineering and Instrumentation **70C**(4), 275–280 (1966)